scientific reports

Check for updates

OPEN

Unveiling the potential of direct synthesized PbS CQD ink based solar cells through numerical simulation

Batuhan Uzun[1,2] & Demet Asil[1,2,3]✉

Studies on lead sulfide-PbS quantum dot-QD based solar cells have gained considerable attention in recent years. A direct synthesis-DS method has emerged that makes it possible to obtain PbS ink in a single step by eliminating complex synthesis and ligand exchange processes, thus reducing the production cost and time. However, the limited number of studies on cells obtained with this method obscures the high potential of this technique. In this study, various electron-ETL and hole transport layers-HTL were systematically brought together in the SCAPS-1D environment to determine the architecture of the cell with record performance. A photoconversion efficiency-PCE of over 20% was achieved with a cell in which n-type DS PbS inks were combined with TiO_2 ETL and MoO_3 HTL. Moreover, we found that p-type DS PbS inks have a much higher potential than n-type inks, with a PCE of up to 36%, and most importantly, they are more resistant to increased defect density. We believe that this study, in which the device architecture for DS PbS inks was optimized and structured for the first time and the importance of p-type DS PbS inks was emphasized, will shed light on future studies in the field of solar cell technologies.

Studies in the field of Si-based solar cells, which are theoretically expected to reach a maximum cell efficiency of 33%, have yielded results and an efficiency of approximately 26.8% has been achieved[1,2]. However, the need for relatively more cost-effective, durable and highly efficient solar cell technology is increasing day by day. Although crystalline silicon (c-Si) technology has reached a mature stage, rising costs remain a constant concern. Therefore, it is of great importance to determine semiconductor materials and device architectures that can meet this need. Lead chalcogenide (PbX, X: S, Se, Te) nanocrystals (NCs), on the other hand, are considered as prominent candidates due to their low-cost synthesis, high bandgap tunability, multiple exciton generation effect, and high device stability for many optoelectronic applications such as photovoltaic (PV) applications, flexible and light-weight optoelectronic devices, NIR and SWIR imagers[1,3].

Various methods have been applied to synthesize lead sulfide (PbS) colloidal quantum dots (CQDs)[4,5]. The most studied method among them is known as hot injection method which have led many photovoltaic and optoelectronic devices. The synthesis of PbS CQDs with this method typically involves the utilization of precursors containing long-alkyl chain surfactants, acting as surface ligands for the CQDs. While these organic surfactants enable precise manipulation of the optical and morphologies properties of the CQDs, the long ligands impede electronic transport between CQDs, resulting in suboptimal device performance[6,7]. To overcome this problem, two main ligand exchange strategies have been developed. One of them is the Layer by Layer (LBL) process which is carried out in solid phase and requires time consuming deposition processes[8,9]. The second approach is known as the solution phase ligand exchange method, and it allows single step deposition by converting PbS CQDs into an ink form[10,11]. Yet, for both strategies, the initial hot injection process is still required and complex ligand-exchange processes remain as a challenge[12]. Recently, a new method, called direct synthesis (DS) technique, has been introduced for which the hot injection step is not required and allows the preparation and deposition of PbS CQD inks in one step[13]. Additionally, DS method reduces the PbS CQD ink cost down to 6$ g^{-1} whereas the cost of PbS CQD inks prepared by solution phase ligand exchange method is estimated to be higher than $16g^{-1}$[13].

Extensive research conducted on the DS PbS method have predominantly been focused on the synthesis optimization and photodiodes with similar device architectures have been fabricated; here, zinc oxide (ZnO)

[1]Department of Micro and Nanotechnology, Middle East Technical University, Ankara 06800, Turkey. [2]METU-MEMS Center, Ankara 06530, Turkey. [3]Department of Chemistry, Middle East Technical University, Ankara 06800, Turkey. ✉email: ademet@metu.edu.tr

was chosen as the Electron Transport Layer (ETL) and ethane-1,2-dithiol (EDT) exchanged PbS (PbS-EDT) was used as the Hole Transport Layer (HTL). According to the previous reports, the main motivation behind this ETL choice was that PbS-EDT effectively performs surface passivation and, as a result, allows high open circuit voltage (V_{OC}) values to be achieved. However, it is known that low charge transport characteristics and mobility negatively affect the performance parameters of the CQD-based solar cells, and therefore the search for the optimum HTL layer still continues[14]. Generally used HTLs are inorganic (e.g. CuI, CuSCN, NiO) or polymeric (e.g. PEDOT: PSS) materials. Inorganic HTLs are cost effective and reported to be more stable under atmospheric conditions[15]. On the other hand, polymeric HTLs are water resistant and compatible with the other cell components[16]. Similarly, ETLs are another important cell component. Owing to their better band alignment and high mobility, materials like ZnO, SnO_2 and TiO_2 are widely used as an ETL in PbS CQD based solar cells. As a result of these studies, the efficiency of solar cells with ITO/ZnO/DS PbS Ink/PbS-EDT/Au architecture produced by the n-type DS PbS ink method has reached a remarkable efficiency in the range of 12.12%[17]. However, since the effects of different ETL-HTL combinations on device performance are not yet known, the potential of these solar cells has not yet been fully revealed. In this study, several simulations were systematically conducted on DS PbS ink based solar cells for the first time to reveal the effect of different ETL-HTL combinations on cell performance. In addition, previous reports showed that the type of doping profile has a significant impact on PV performance[18]. For the inks derived from solution phase ligand exchanged technique, Choi et al. reported that p-type inks could be produced via cascade surface modification strategy where n-type CQD surfaces were reprogramed with functional ligands such as cysteamine and 1-thioglycerol[18]. Solar cells using these p-type inks as the light-harvesting active layer showed relatively higher cell performance compared to n-type inks[18]. In accordance with these promising results for the p-type inks, Liu et al., developed a strategy which gives a more p-type characteristics to the DS PbS inks. This was achieved by adding monofunctional or bifunctional thiol molecules to the lead iodide precursor solution in dimethyl formamide (DMF), before the butylamine (BA) injection[19]. They found that 1-propanethiol molecule imparted a more dominant p-type character to DS inks than 3-mercaptopropionic acid, but they focused on the n-type DS inks for further PV studies. They reported that solar cells using these n-type DS inks achieved a photoconversion efficiency (PCE) in the range of 13.3%[19]. Consequently, since the current synthetic approach used for DS PbS inks allows limited control over dopant type and concentration, solar cells produced based on this approach appear to incorporate traditionally used n-type inks. For this reason, the potential of p-type DS inks in solar cells has not yet been revealed. Research on synthesizing p-type PbS inks is still in its early stages and continues to evolve. In particular, ligand-exchange methods developed for p-type CQD inks have led to surface defects. These defects arise from the steric hindrance of the doping ligands which limits complete surface coverage[18]. Moreover, Choi, M. et al. reported that the p-type PbS ink has larger inter-dot spacing and lower electron mobility compared to n-type ink due to those limitations. Additionally, it has been demonstrated that n-type CQD inks disperse more effectively in butylamine (BTA) due to the presence of surface lead halides[18]. In contrast, the solubility of p-type inks in colloidal form is affected by the secondary functional groups in thiol ligands (–L in SH–R–L). This is due to the formation of strong bonds between the thiol groups and the CQD surface, which leads to a limitation in the solubility of p-type inks. Despite these drawbacks, p-type ink demonstrated better performance in terms of fill factor (FF), short circuit current density (J_{SC}), and V_{OC} and this was attributed to its higher photoluminescence performance and lower nonradiative recombination rate[18]. Even the limitations of the p-type PbS ink due to its infant synthesis stage, its potential is encouraging. In this context, it is important to uncover the potential of p-type inks.

In this study, for the first time, several simulations were systematically conducted on DS PbS ink based solar cells to reveal the effect of different ETL-HTL combinations on the cell performance. The DS PbS ink-based ITO/ZnO/DS PbS Ink/PbS-EDT/Au solar cell architecture was used as the control cell, and the PV parameters obtained from simulations using this architecture were compared with the experimental results to verify the DS PbS ink SCAPS 1-D (Solar Cell Capacitance Simulator) parameters used in this study[13]. PCE in the range of 20.24% was achieved for ITO/TiO_2/DS PbS Ink/MoO_3/Au architecture. Moreover, this champion cell architecture was simulated for both p-type and n-type ink scenarios to reveal the true potential of the champion device architecture. In addition, we investigated the simultaneous effects of defect density (varied from 10^{13} to 5×10^{16} cm^{-3}) and dopant type of the DS PbS ink where the dopant concentration was varied from 10^{13} to 10^{22} cm^{-3}. We found that the p-type ink in this structure makes the device more resilient in terms of PCE against the changes in defect density. To understand the effect of doping type on the PV parameters further, we changed the thickness of the ink from 100 to 600 nm for both n-type and p-type inks where their dopant concentrations were varied from 10^{13} to 10^{22} cm^{-3}. In line with previous reports, we found that the cell with p-type ink showed higher performance regardless of dopant concentration and thickness. According to our simulation studies, we observed that the champion solar cell architecture containing p-type ink can reach a very high PCE of around 36.40% when the dopant and defect concentration are 10^{22} cm^{-3} and 10^{13} cm^{-3}, respectively. We believe that our study examining various solar cell architectures based on various combinations of ETL and HTL and different types of DS PbS inks (n or p-type) and reporting promising PCE values will play an important role in determining the focus of future research in this field.

Device structure and method

The numerical analysis was conducted in SCAPS-1D tool for one-dimensional simulations, developed by Department of Electronics and Information Systems (ELIS) of the University of Gent, Belgium[20]. Utilizing the SCAPS-1D simulation tool, one can compute current/voltage characteristics, photovoltaic parameters, quantum efficiencies, dopant density profiles, total generation/recombination profiles, along with corresponding energy band diagrams, among other factors. The tool operates on the principles of the one-dimensional Poisson's

equation in semiconductors, carrier continuity (electron/hole transport), and the drift-diffusion differential equations[21]. Poisson's equation and continuity relations for holes and electrons as follows:

$$\frac{d}{dx}\left(\epsilon\ (x)\frac{d\psi}{dx}\right) = q[p\,(x) - n\,(x) + N_{D^+}\,(x) - N_{A^-}\,(x) + p_t\,(x) - n_t\,(x)] \quad (1)$$

$$\frac{1}{j}\frac{dJ_n}{dx} + R_n\,(x) - G\,(x) = 0 \quad (2)$$

$$\frac{1}{j}\frac{dJ_p}{dx} + R_p\,(x) - G\,(x) = 0 \quad (3)$$

Here, ε(x) denotes the permittivity at the position within the device x, while ψ and q represent the electrostatic potential and electron charge. Symbols n and p signify the concentrations of free electrons and holes, and N^+_D and N^+_A represent the ionized concentrations of donor-like and acceptor-like dopants. Additionally, n_t and p_t denote trapped electrons and holes, J_n and J_p are the current densities of electrons and holes, G(x) represents the photogeneration rate, and R_n(x) and R_p(x) are defined as the electron and hole recombination rates, respectively.

To determine the best HTL and ETL combination, in this study, systematic simulation studies were conducted using ETLs and HTLs having different band alignments (see Fig. S3). Several HTLs (see Table 1) such as PbS-EDT, poly(ethylene-3,4-dioxythiophene): poly(styrenesulfonic acid) (PEDOT: PSS), copper (I) iodide (CuI), copper (I) oxide (CuO), copper (II) oxide (Cu_2O), copper(I) thiocyanate (CuSCN), molybdenum trioxide (MoO_3), nickel oxide (NiO) and 2,2′,7,7′-Tetrakis[N, N-di(4-methoxyphenyl)amino]-9,9′-spirobifuorene (Spiro-MeOTAD) were used. On the other hand, as summarized in Table-2, various types of ETLs such as ZnO, titanium dioxide (TiO_2), tin (IV) oxide (SnO_2), indium gallium zinc oxide (IGZO), fullerene (C_{60}), cadmium sulfide (CdS) and cerium (IV) oxide (Ce_2O) were utilized as the ETLs. To achieve realistic simulation and analysis of semiconductor devices, it is essential to integrate accurate and reliable optoelectronic properties for all the materials employed in the simulation. In this respect, SCAPS parameter values were obtained from past studies and a significant focus was placed on optimizing various parameters to gain a comprehensive understanding of the device performance. Tables 1 and 2 summarize the complete list of SCAPS parameter values used throughout the simulation studies.

For DS PbS ink layer, the absorption coefficient (α) was derived through our experimental study, following the methods outlined in literature, meanwhile, the remaining SCAPS parameters were collected from previously reported experimental studies[13,17]. To prepare the control DS PbS inks, lead iodide (6 mmol) and diphenyl thiourea (1 mmol) were dissolved in dimethyl formamide (9 mL) while stirring under nitrogen at room temperature. Once all solids were dissolved, butylamine (1 mL) was swiftly injected, causing the solution to promptly turn black. Following this, toluene was introduced as an anti-solvent, and the PbS CQDs were subsequently centrifuged for 10 min at 5000 rpm. In general, the fabrication of solar cells involves sequentially spin-coating of the ETL (ZnO), active layer (DS PbS ink) and HTL (PbS QDs ligand exchanged with EDT)

Parameters	Active material	Hole transport layers								
	DS PbS ink[13]	PbS-EDT[19,21]	PEDOT: PSS[22,23]	CuI[22,24]	CuO[22,25]	Cu_2O[22,26–28]	CuSCN[22,26]	MoO_3[29–31]	NiO[22,32–34]	Spiro-MeOTAD[21,22]
Thickness (nm)	300[a]	50	50	50	50	50	50	50[a]	50	50
Bandgap (eV)	1.4	1.4	1.6	3.1	1.51	2.17	3.6	3	3.6	3
Electron affinity (eV)	4	3.5	3.4	2.1	4.07	3.2	1.7	2.5	1.8	2.2
Dielectric permittivity	19.8	20	3	6.5	18.1	7.1	10	12.5	11.7	3
CB effective density (cm^{-3})	10^{19}	10^{19}	2.2×10^{18}	2.8×10^{19}	2.2×10^{19}	2×10^{17}	2.2×10^{19}	2.2×10^{18}	2.5×10^{20}	2.2×10^{18}
VB effective density (cm^{-3})	10^{19}	10^{19}	1.8×10^{19}	10^{19}	5.5×10^{20}	1.1×10^{19}	1.8×10^{18}	1.8×10^{19}	2.5×10^{20}	1.8×10^{19}
Electron thermal velocity (cm/s)	10^7	10^7	10^7	10^7	10^7	10^7	10^7	10^7	10^7	10^7
Hole thermal velocity (cm/s)	10^7	10^7	10^7	10^7	10^7	10^7	10^7	10^7	10^7	10^7
Electron mobility (cm^2/V s)	2.67×10^{c2}	2×10^{-4}	4.5×10^{-2}	100	100	200	100	25	2.8	2.1×10^{-3}
Hole mobility (cm^2/V s)	2.67×10^{-2}	20	4.5×10^{-2}	43.9	0.1	80	25	100	2.8	2.16×10^{-3}
Shallow uniform donor density N_D (cm^{-3})	8.77×10^{16a}	10^{14}	0	0	0	0	0	0	0	0
Shallow uniform acceptor density N_A (cm^{-3})	0[a]	10^{16}	10^{18}	10^{18}	10^{18}	10^{18}	10^{18}	10^{18}	3×10^{18}	10^{18}
Defect density (cm^{-3})	10^{14}	10^{15}	10^{15}	10^{15}	10^{15}	10^{15}	10^{15}	10^{15}	10^{15}	10^{15}

Table 1. Simulation parameters of the light absorbing active material (DS PbS ink) and various types of hole transport layers. [a]The optimized values for the champion cell were found through simulation. For MoO_3 HTL, the optimum thickness was found to be 50 nm. For p-type inks, the optimum thickness and N_A were found to be 400 nm 10^{22} cm^{-3}, respectively. For n-type inks, the optimum thickness and N_D were found to be 300 nm 10^{13} cm^{-3}, respectively.

Parameters	Electron transport layers						
	ZnO[22,35]	TiO_2[22,36]	SnO_2[37]	IGZO[22]	C_{60}[22,38]	CdS[35,39]	CeO_2[22]
Thickness (nm)	100	100	100	100	100	100	100
Bandgap (eV)	3.3	3.2	3.6	3.05	1.7	2.4	3.5
Electron affinity (eV)	4.2	4.26	4.5	4.16	4.5	4.5	4.6
Dielectric permittivity	9	9	9	10	6	10	9
CB effective density (cm^{-3})	3.7×10^{18}	2.2×10^{18}	2.2×10^{18}	5×10^{18}	10^{19}	1.5×10^{18}	10^{20}
VB effective density (cm^{-3})	1.8×10^{19}	1.8×10^{19}	1.8×10^{19}	5×10^{18}	10^{19}	1.8×10^{18}	2×10^{21}
Electron thermal velocity (cm/s)	10^7	10^7	10^7	10^7	10^7	10^7	10^7
Hole thermal velocity (cm/s)	10^7	10^7	10^7	10^7	10^7	10^7	10^7
Electron mobility ($cm^2/V{\cdot}s$)	100	20	100	15	50	50	100
Hole mobility ($cm^2/V{\cdot}s$)	25	10	25	0.1	50	20	25
Shallow uniform donor density N_D (cm^{-3})	10^{18}	10^{19}	10^{20}	10^{17}	10^{18}	10^{17}	10^{21}
Shallow uniform acceptor density NA (cm^{-3})	0	0	0	0	0	0	0
Defect density (cm^{-3})	10^{15}	10^{15}	10^{15}	10^{15}	10^{15}	10^{15}	10^{15}

Table 2. Simulation parameters for the electron transport layers.

onto an ITO substrate, followed by the deposition of the final contact layer (Au) using thermal evaporation technique. For the remaining materials, α was obtained from the in-built model in SCAPS, $\alpha = A_\alpha (h\nu E_g)^{1/2}$ where $A_\alpha \sim 10^5$, E_g represents bandgap, and ν is the frequency. In order to achieve cell performance parameters similar to the reported studies, the neutral interface defects with 10^{-18} cm^{-2} electron and hole capture cross section where the reference defect level above the highest E_v of 0.6 eV were also added between the ETL/DS PbS ink and DS PbS ink/HTL layers. For the rest of the layers such as back contact metallic gold (Au) (which has work function − 5.1 eV) and front contact indium-tin-oxide (ITO) (which has work function − 4.7 eV)[40–43], the surface recombination velocities of electron and hole were set as 10^5 cm s^{-1} and 10^7 cm s^{-1}, for Au contact and 10^7 cm s^{-1} and 10^5 cm s^{-1} for ITO contact respectively[41,44,45].

Results and discussion

Verification of SCAPS parameters

One of the conventional device architectures that has been experimentally successful so far is ITO/ZnO/DS PbS ink/PbS-EDT/Au; where DS PbS ink serves as the main absorber layer, ZnO serves as the ETL, and PbS-EDT serves as the HTL. Based on a recently reported study by Wang et al., this device structure achieved a very promising PCE in the range of 10.1%[13]. Therefore, we used this cell architecture as a control cell to validate our SCAPS parameters given in Tables 1 and 2. The general device structure used throughout the simulation studies is illustrated in Fig. 1a. To implement the absorption spectrum of the light absorbing active material to the SCAPS environment, DS PbS QD ink was synthesized following the previously reported methods[13,17]. Figure 1b shows the thin film absorption spectrum of the DS PbS ink which has an absorption edge at around 1000 nm. Moreover, we characterized the surface morphology of the DS PbS ink layer over an area of 2.5 µm x 2.5 µm using atomic force microscopy (AFM). As represented in Fig. S1, thin film has a smooth surface with root mean square (rms) roughness in the range of 0.8 nm. Figure 1c and d show the current density-voltage (J-V) behavior and external quantum efficiency (EQE) spectrum of the simulated cell in the SCAPS environment. The choice of parameters used in SCAPS for this study was based on previous SCAPS simulations reported in the literature. Specifically, the material parameters such as bandgap energy, electron affinity, dielectric constant, and effective density of states were chosen to align with values commonly used in well-established SCAPS studies, ensuring consistency and comparability with prior work. For the defect density parameters in the active layer, we adopted values from actual experimental reports and studies (see Fig. S2 for further details). These parameters were selected to accurately reflect the defect states and trap levels observed in real-world materials, providing a realistic simulation of the electronic behavior of the device. This approach ensures that the defect density parameters closely represent the material's quality and properties as reported in empirical studies, enhancing the relevance and reliability of the simulation results.

To demonstrate the accuracy of the absorption spectrum shown in Fig. 1b and the validity of the SCAPS parameters summarized in Tables 1 and 2, the cell parameters simulated in the SCAPS environment in this study were compared with the device parameters reported in past studies. These comparative results, summarized in Table 3, show that we achieved cell parameters very close to the control cell reported in previous studies and confirm the SCAPS parameters we used in the simulation studies. Compared to experimental results, lower J_{SC} and FF were observed in SCAPS simulations for direct synthesized (DS) PbS ink-based solar cells. In line with literature, this was attributed to the simplified assumptions used for defect modeling due to the lack of detailed experimental data defining defect types in these cells[46]. Although previous reports showed that trap-assisted processes can positively impact J_{SC} and FF by facilitating charge separation and transport, reducing recombination, and improving carrier extraction, we carried out our simulations by adding neutral defects with Gaussian distribution to make them more consistent and reliable[47]. We believe that this discrepancy between simulation and experimental parameters highlights the need for more comprehensive experimental studies to

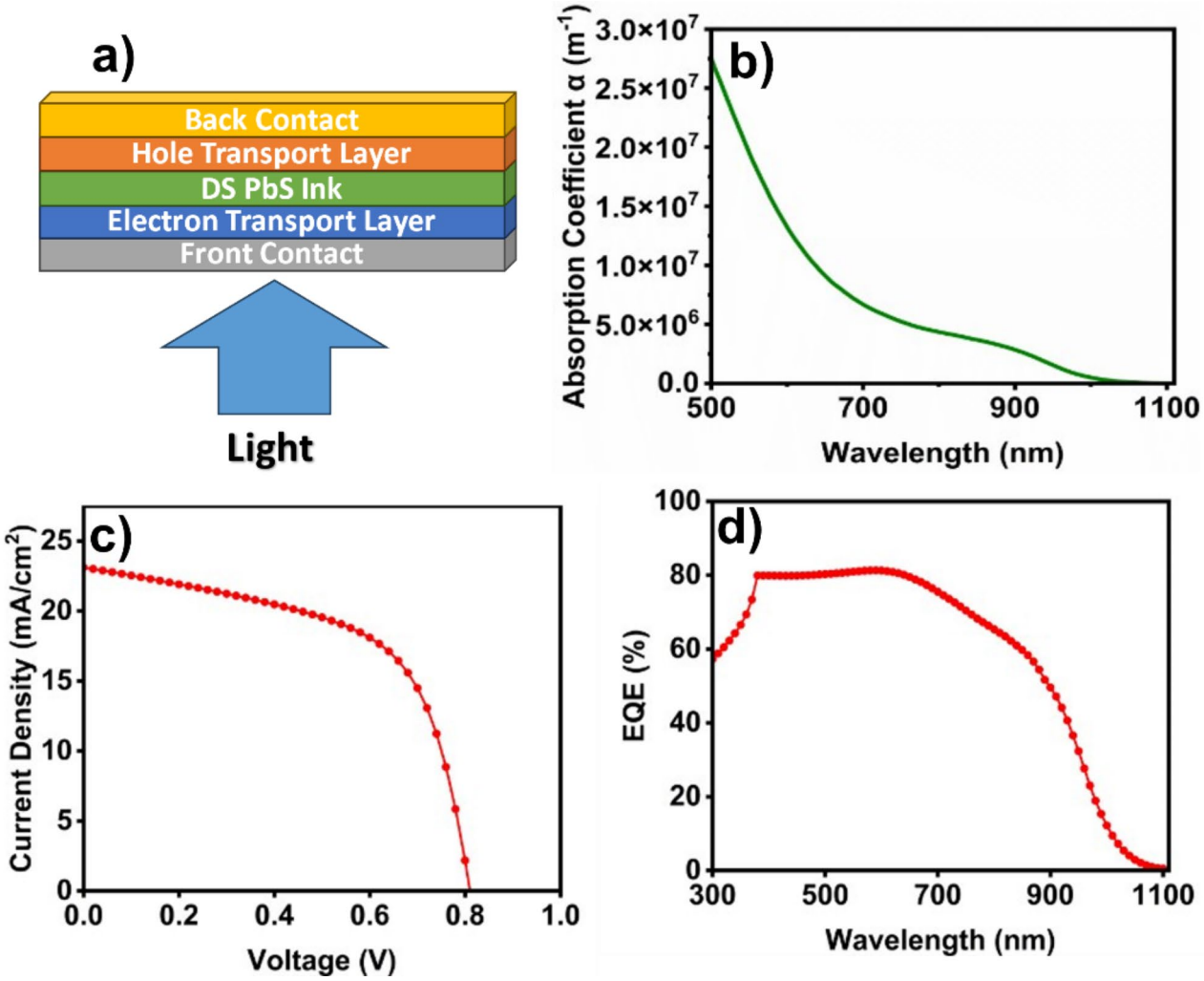

Fig. 1. Verification of the SCAPS parameters. (**a**) Representation of the device structure. (**b**) Thin film absorption spectrum of the as synthesized DS PbS ink. (**c**) J–V diagram and (**d**) EQE spectrum of the simulated ITO/ZnO/DS PbS ink/PbS-EDT/Au control cell.

	V_{OC} (V)	J_{SC} (mA cm^{-2})	FF (%)	PCE (%)
Control cell[13]	0.63	25.1	64.0	10.1
Simulated in this study	0.81	23.1	58.5	10.9

Table 3. Comparison of SCAPS simulation results with cell parameters obtained from experimental studies. Cell architecture is ITO/ZnO/DS PbS ink /PbS EDT/Au.

better define defect types and their impact on device performance, enabling more accurate simulations for future studies.

Effect of different ETL-HTL combinations on solar cell performance parameters

To determine the best ETL-HTL combination for DS PbS ink based solar cells, 63 different device structures were simulated and solar cell parameters are summarized in Fig. 2. Considering all ETL-HTL combinations, it was determined that devices containing MoO_3 material as HTL exhibited significantly higher performance than the others. On the other hand, significant efficiencies of over 18% were achieved for multiple ETL materials used in the simulation studies. Solar cells where ZnO (Fig. 2a), TiO_2 (Fig. 2b) and IGZO (Fig. 2c) were used as the ETL and MoO_3 as the HTL achieved 20.03%, 20.24% and 18.66% PCE, respectively. On the other hand, it was found that relatively lower performance parameters were obtained when MoO_3 HTL material was combined with ETLs such as SnO_2 (Fig. 2d), C_{60} (Fig. 2e), CdS (Fig. 2f), and CeO_2 (Fig. 2g). Notably higher and very similar PCE values obtained for ZnO (Fig. 2a) and TiO_2 (Fig. 2b) ETLs led us to focus on ITO/ZnO/DS PbS ink/MoO_3/Au or ITO/TiO_2/DS PbS ink/MoO_3/Au structure for the rest of our study. To determine the best

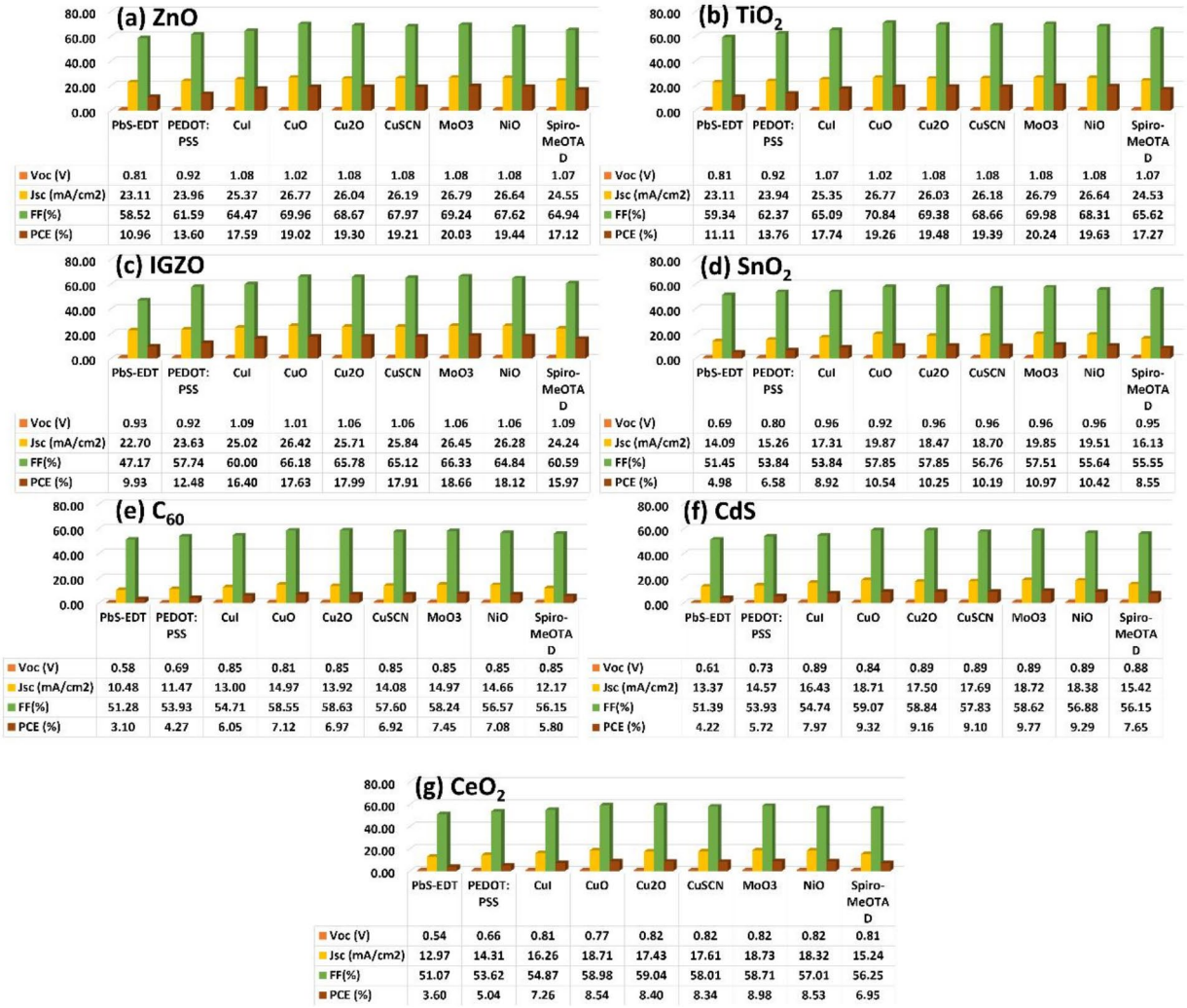

Fig. 2. Solar cell parameters for 63 different ETL-HTL combinations. Various ETLs (thickness = 100 nm) and HTLs (thickness = 50 nm) were combined with DS PbS ink active layer (thickness = 300 nm) where ETLs are: (**a**) ZnO, (**b**) TiO_2, (**c**), (**d**) IGZO, (**d**) SnO_2, (**e**) C_{60}, (**f**) CdS, (**g**) CeO_2.

candidate for the ETL material, a deeper analysis was carried out for the ETL (see Fig. S4 and Fig. S5). We found that TiO_2 has a notably higher electron extraction rate as compared to ZnO due to its lower electron quasi fermi level. Therefore, TiO_2 was chosen as the ETL throughout this study.

When we compared the performance of solar cells containing several HTL materials (thickness was set as 50 nm) with different properties, we found that the choice of HTL has a profound effect on the cell parameters. To understand the underlying reasons, we investigated the generation and recombination characteristics of the simulated cells. Figure 3a and b show the generation and recombination profiles within the cell, respectively. We found that the generation rate follows; PbS-EDT > CuI > PEDOT: PSS > Cu_2O > CuSCN > NiO > MoO_3 > CuO > Spiro-MeOTAD. As shown in Fig. 3a, widely used PbS-EDT HTL demonstrates significantly higher generation rate among all the other HTLs. However, with 11% PCE, it was the worst performing HTL when it was combined with TiO_2 (see Fig. 2b).

The underlying reasons behind this poor performance were investigated by simulating the recombination profiles. Figure 3b shows the variation of the recombination rate within the device. We found that the recombination rate sequence is as follows: PbS-EDT > PEDOT: PSS > CuI > Cu_2O > CuSCN > NiO > Spiro-MeOTAD > MoO_3 > CuO. When two different sequences obtained in recombination and production rates are examined, it is seen that these two processes are two competing processes that directly affect the performance parameters in the solar cell. Despite the high production rate achieved for PbS-EDT, the recombination rate, which was found to be equally high, led us to conclude that this HTL material may not be the optimum HTL for this device architecture. This is clearly seen in Fig. 2; PbS-EDT HTL has significantly lower J_{SC} and V_{OC} when used not only with TiO_2 ETL but also with all other ETL materials. Possible reasons for the relatively low J_{SC} and sources of the losses were investigated through EQE profiles. Figure 3c shows the simulated EQE spectra for cells where ETL was set to TiO_2 and HTL was varied. Accordingly, it was concluded that the EQE profile is strongly affected by the HTL selection and J_{SC} losses are mainly caused by photocurrent loss in the visible region (400–

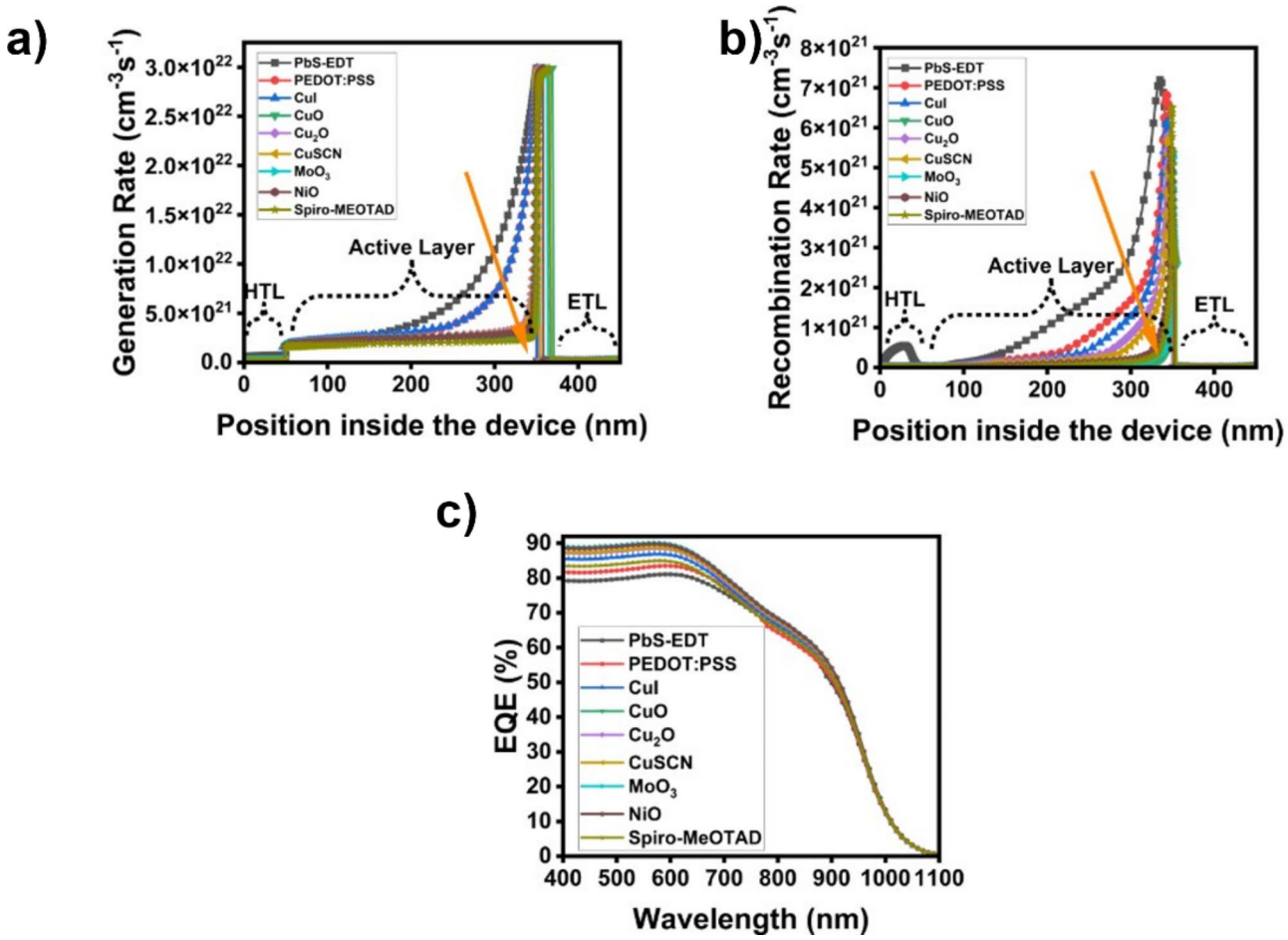

Fig. 3. Effect of HTL on the generation and recombination profile. Simulated (**a**) generation rate, (**b**) recombination rate, and (**c**) EQE spectra of the solar cells with ITO/TiO_2 (100 nm)/DS PbS ink (300 nm)/HTL (50 nm)/Au device architecture.

700 nm). Compared to other HTL materials, MoO_3 showed minimal photocurrent loss in this range; this was mainly attributed to its relatively lower recombination rate compared to others. This superior performance of MoO_3 can be attributed to its favorable energy band alignment with the absorber layer, which reduces the energy barrier for hole extraction and improves charge separation (Fig. S3). Its high electron affinity effectively blocks electrons, minimizing recombination at the HTL interface and enhancing charge selectivity, resulting in higher V_{OC} and FF. Additionally, MoO_3's low density of surface states leads to lower recombination rates, while its stable and uniform interface with absorbers reduces degradation, ensuring better device longevity[29]. Thus, having a much lower recombination rate compared to other HTLs[48], being compatible in terms of band alignment with DS PbS ink (Fig. S3), and having the highest hole mobility value among the other HTLs (Table 1), MoO_3 can be considered as an ideal hole transport layer for the DS PbS ink based solar cells.

As a result, the champion solar cell architecture was determined as ITO/TiO_2 (100 nm) /DS PbS ink (300 nm) /MoO_3 /Au; where ETL was TiO_2 and HTL was MoO_3. Additionally, to investigate the effect of MoO_3 HTL thickness on the cell performance, the MoO_3 thickness was changed between 10 and 100 nm and its effects on cell parameters were examined. Although a minimal increase in PV performance parameters (J_{SC} and FF) was observed between 10 and 50 nm, as shown in Fig. S6, this effect was observed to reach a plateau as the HTL thickness increased above 50 nm. Therefore, the HTL thickness was set to 50 nm for future simulation studies.

Investigating the characteristic properties of the champion cell: concurrent effects of dopant type/concentration and defect density

PbS-QD based solar cells have not yet reached the desired PCE values due to the presence of defects induced during synthesis and/or solar cell fabrication steps[49]. Therefore, examining the sources of defects and their possible effects on the cell performance and developing strategies to prevent these defects are the most effective tools to overcome this bottleneck. On the other hand, dopant type and concentration are other parameters that affects the final cell yield[21]. In DS PbS CQD inks, defects mainly arise from incomplete surface passivation, structural irregularities, precursor impurities, and solvent interactions. Surface defects occur when iodoplumbate complexes (e.g., PbI_3^-, PbI_4^{2-}) used for passivation fail to fully cover QD surfaces, leaving undercoordinated Pb or S atoms that act as trap states[13]. Rapid nucleation and growth during synthesis can also cause non-uniform

QD sizes, leading to structural defects like dislocations or vacancies. Impurities in precursors such as PbI_2 or DPhTA can introduce additional defects, while solvents like DMF or DMSO may interfere with surface passivation[17]. The interaction of dopants with these defects depends on their type and concentration. While n-type dopants, such as iodide, may help to passivate Pb-rich surface sites, excess iodide may also introduce shallow donor states that might act as new trap states. p-type dopants, on the other hand, passivate S-rich sites by reducing sulfur vacancies but may also introduce acceptor states that might trap holes. Moreover, the size and binding strength of the dopant molecules have significant effects on the passivation; larger or strongly binding dopants may provide better passivation but have risk of steric hindrance or destabilizing the colloidal stability[17,50]. As achieving optimal properties in PbS CQD inks requires balancing defect passivation and dopant levels, controlling synthesis conditions, precursor purity, and dopant concentration is essential to minimize defect density and enhance the performance of PbS CQD-based devices.

Additionally, the existence of studies confirming the potential of p-type PbS CQD inks to achieve promising cell efficiencies compared to their n-type counterparts led us to investigate how the PV parameters would change if the DS PbS inks were p-type. Thus, to explore the response of the cell against defects for both dopant types, DS PbS ink was simulated at various dopant concentrations over different defect densities. Figure 4 demonstrates concurrent effects of dopant type/concentration and defect density on the cell parameters. During this simulation, the thickness of the DS PbS ink layer was fixed at 300 nm, the acceptor and donor concentrations and the defect density were varied from 10^{13} to 10^{22} cm^{-3} and 10^{13} to 5×10^{16} cm^{-3}, respectively.

In line with previous studies, we found that V_{OC} decreases as the defect density increases regardless of the dopant type (see Fig. 4a and b)[22]. Similarly, it was observed that as the doping concentration in the active layer increases, V_{OC} increases for both for n-type and p-type DS PbS inks (see Fig. 4a and b). This behavior, known to have detrimental effects on the FF and PCE, was attributed to the reduction in the reverse saturation current with an increase in the dopant concentration[51]. Similar trends observed for V_{OC} versus increase in defect concentration were also noted for J_{SC}. Based on the simulation results shown in Fig. 4c and d, and in agreement with previous reports, it was observed that J_{SC} decreases as the defect concentration increases for both types of dopants[21]. Interestingly, we found that the effect of dopant concentration on J_{SC} cannot be evaluated independently of the defect concentration. For both dopant types, higher J_{SC} values were recorded at lower dopant concentrations, and this behavior was attributed to the enhanced charge carrier collection rate due to an increase in depletion width[21]. However, we discovered that at higher dopant concentrations, how J_{SC} responds to an increase in defect concentration depends entirely on the dopant type. As shown in Fig. 4d, when the dopant type is p-type, high J_{SC}'s can be achieved even at higher defect densities. Interestingly, when the defect concentration was below 10^{14} cm^{-3}, p-type ink solar cells were observed to have higher J_{SC} values than their n-type counterparts at higher dopant concentrations. Additionally, we noted that FF follows similar patterns for both dopant types; it increases with decreasing defect concentration and increases with increasing dopant concentration (Fig. 4e and f). As a result, the highest PCE value for an n-type ink (over 26%) could be reached at lower dopant concentrations (below 10^{18} cm^{-3}) (Fig. 4g), while when the dopant type was p-type, the highest PCE (over 30%) could be reached at higher dopant concentrations (above 10^{20} cm^{-3}) (Fig. 4h). In line with past studies, we discovered that p-type inks always outperform their n-type counterparts under the same conditions.

It was expected that the depletion width would decrease with increasing dopant concentration and thus the PCE would decrease with a decrease in J_{SC} (Fig. 4g)[52]. However, unlike n-type inks, p-type inks unexpectedly showed higher performance at higher dopant concentrations (Fig. 4h). To further investigate the source of this unexpected result, the electrical field intensity within the device was simulated at a fixed defect density (10^{13} cm^{-3}). In accordance with previous reports, we found that higher acceptor concentration leads to a higher electric field and thus increases the carrier extraction rate[53]. To explore this effect, we applied Mott-Schottky analysis and determined the behavior of depletion width with respect to acceptor concentration (see Fig. S6).

Concurrent effects of acceptor concentration and voltage on the depletion width are represented in Fig. 5a. As expected, simultaneous increase in voltage and acceptor concentration leads to a decrease in the depletion width. However, as we mentioned before, this trend in depletion width does not explain unexpectedly higher performance achieved by the p-type inks at higher acceptor concentrations. This led us to further investigate whether this phenomenon was observed due to the differences in the generation and recombination rates. Figure 5b and c represent the variation of the generation and the recombination profiles against acceptor concentration. We found that the generation rate is maximized (at 3×10^{22} cm^{-3}) inside the p-type DS PbS ink layer near to the TiO_2 side and the position of the max generation rate shifts towards the HTL side as the acceptor concentration increases (see Fig. 5b). Similar trends were observed for the recombination rate; while the recombination rate is maximized 6×10^{20} $cm^{-3}s^{-1}$ in the p-type active layer close to the ETL side, the position shifts towards the HTL side as the acceptor concentration increases (see Fig. 5c). However, unlike the generation rate, the recombination rate decreases significantly (down to 1×10^{20} $cm^{-3}s^{-1}$) as the acceptor concentration increases. As a result, we conclude that this significant decrease in recombination rate may explain the observed increase in efficiency with an increase in acceptor concentration. Moreover, we observed a small increment in the recombination rate at higher acceptor concentration (after 10^{17} cm^{-3}). This was attributed to the increased scattering centers being made by dopants ultimately which reduce the carrier mobility[54].

To investigate how electrical field intensity ($|E|^2$) in the device is affected by the generation and recombination profiles, we simulated the distribution of electric field intensity versus acceptor concentration within the cell. As represented in Fig. 5d, as the DS PbS ink becomes more p-type, the peak $|E|^2$ moves away from the n-type TiO_2 and extends into the highly doped active layer. As a result, the high PCE and J_{SC} values achieved for cells containing highly doped p-type inks were attributed to the high $|E|^2$ and low recombination rates within the device. Based on the simulation results, it can be concluded that under these two effects, charge carriers can be separated and collected more effectively. Therefore, the highest performance can be achieved when p-type inks with very high additive concentrations are used. Another advantage of the p-type inks is its higher resistance to

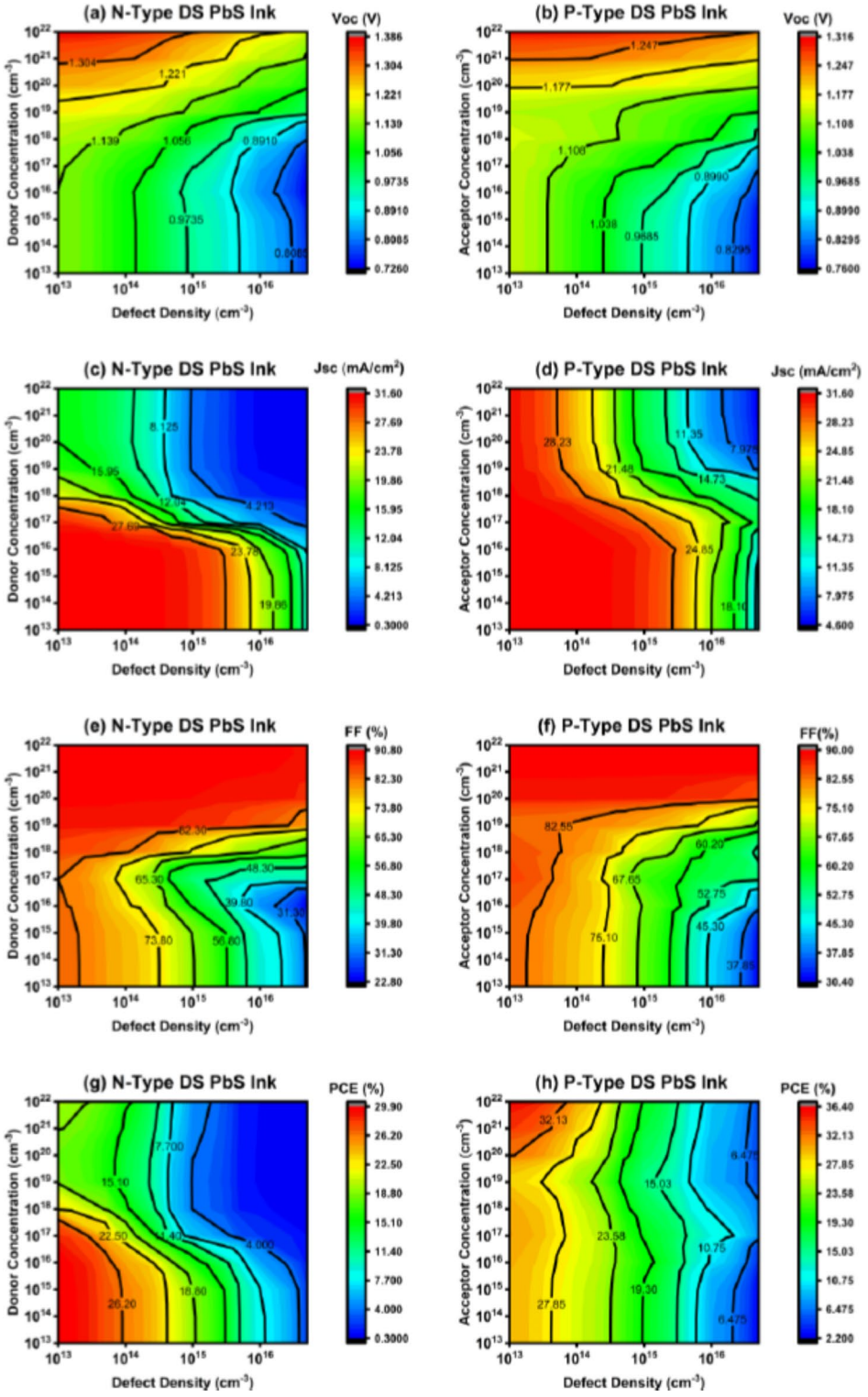

Fig. 4. Concurrent effect of donor/ acceptor concentration and defect density on V_{OC} (**a**, **b**), J_{SC} (**c**, **d**), FF (**e**, **f**), and PCE (**g**, **h**) parameters. The thickness of DS PbS ink was fixed at 300 nm.

the defect density. As shown in Fig. 4g and h, cells using p-type inks can always achieve significantly higher PCE values compared to n-type inks, even with the same dopant concentration and defect densities. Moreover, for all dopant concentration values, the performance parameters of n-type inks show a strong dependence on defect density, while p-type inks remain more unresponsive. As a result, according to our study, the use of p-type inks increases the tolerance of the device against defect density and makes it possible to reach higher PCE values.

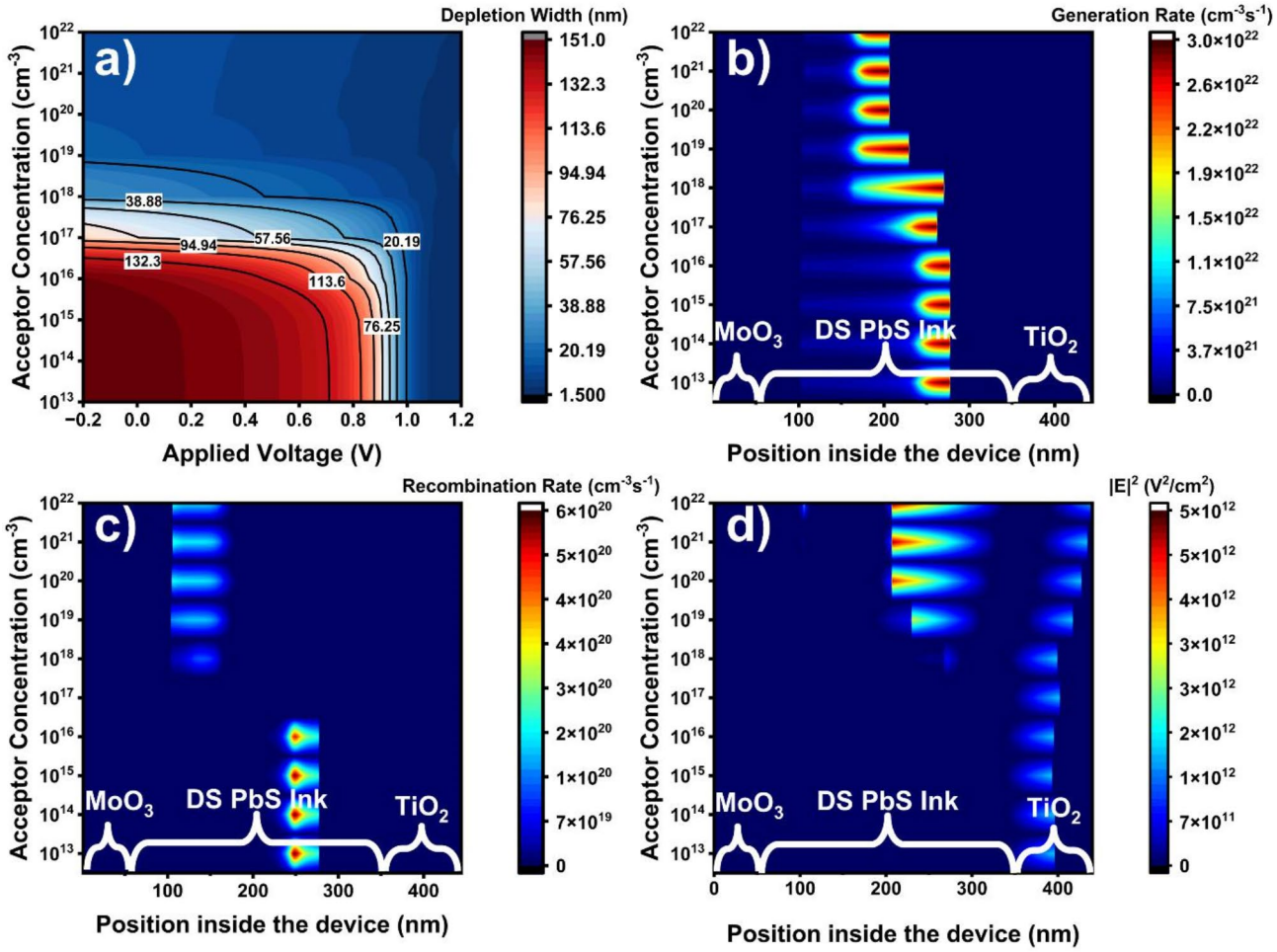

Fig. 5. Concurrent effect of acceptor concentration and voltage on the depletion width and generation, recombination and electrical field intensity profiles in the solar cell. (**a**) Depletion width, (**b**) the generation rate, (**c**) the recombination rate and (**d**) electrical field intensity inside the ITO/TiO_2/p-type DS PbS ink/MoO_3/Au device where the defect density was set at 10^{13} cm^{-3} for the active layer.

Influence of the DS PbS ink thickness on the cell performance

Although we have theoretically demonstrated the relationship between dopant concentration and defects, the effect of active material thickness on PV parameters is another notable parameter that can affect cell performance. Ideally, since the recombination rate increases with the active layer thickness, the diffusion length of the charge carriers should be larger than the thickness of the active layer[40]. On the other hand, if the active layer is too thin, it may lead to insufficient absorption of light and therefore a low photogeneration rate[55]. Therefore, it is critical to determine the optimum thickness for the active layer. In this sense, we simulated the champion cell device architecture for both p- and n-type inks at various active layer thicknesses. We also varied the donor and acceptor concentrations simultaneously to extend our discussion between n-type and p-type DS PbS inks. Figure 6. shows the concurrent effects of donor and acceptor concentrations and the thickness of the active material on solar cell performance parameters for a fixed defect concentration of 10^{14} cm^{-3}.

As shown in Fig. 6a, b and V_{OC} showed similar trends for both ink types, and the maximum achievable V_{OC} value was found to be around 1.3 V. According to the simulation results, while it increases with the donor and acceptor concentration, it decreases slightly as the active layer thickens due to the increase in the carrier diffusion length[56]. Unlike V_{OC}, the increase in the thickness of the active material leads to an increase in J_{SC} for both n and p-type inks as depicted in Fig. 6c and d. As also stated in the previous section, J_{SC} increases as the carrier concentration decreases and this was attributed to the increase in depletion width therefore the generation rate. This time, however, increase in the thickness of the active layer also contributes to the absorption and therefore generation rate. As represented in Fig. 6c and d, regardless of the ink type, we observed that the J_{SC} is less dependent on the dopant concentration at lower thickness. On the other hand, the impact of dopant concentration on J_{SC} becomes more significant when the thickness is above 300–400 nm. We found that FF shows a drastic decrease when donor concentration is lower than 10^{19} cm^{-3} (Fig. 6e) and p-type acceptor concentration is lower than 10^{20} cm^{-3} (Fig. 6f). In line with previous reports, a quasi-neutral region is expected to form with the thickening of the active layer, reducing the overall electric field[57]. The formation of the quasi-neutral region

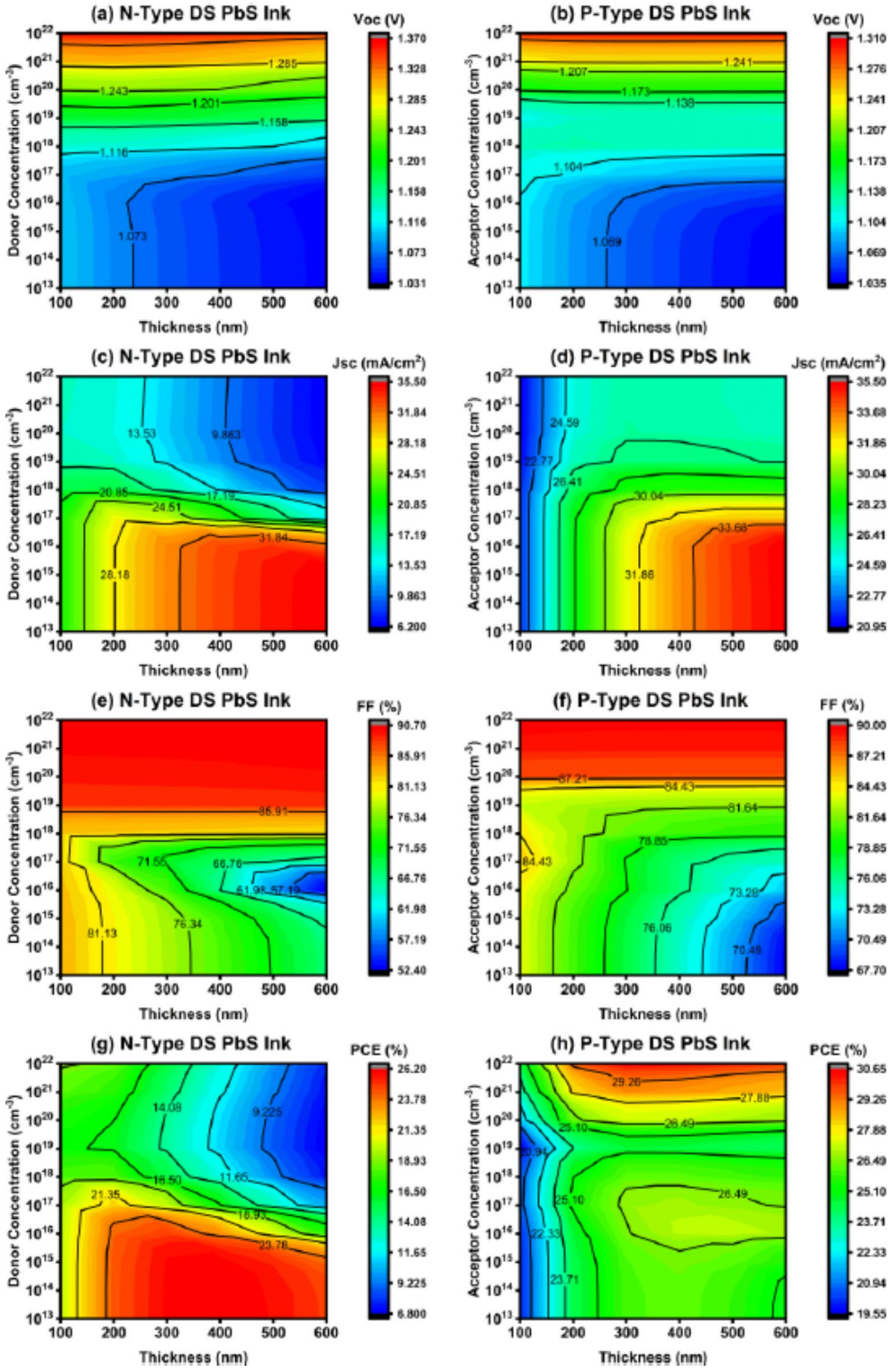

Fig. 6. Concurrent effects of donor and acceptor concentrations and the thickness of the active material on V_{OC} (**a**, **b**), J_{SC} (**c**, **d**), FF (**e**, **f**), and PCE (**g**, **h**) parameters. Defect concentration was fixed at 10^{14} cm^{-3}.

leads to the transport of carriers by diffusion rather than drift, which is expected to reduce the FF by increasing the series resistance. Overall, we found that the p-type DS PbS ink exhibits significantly higher PCE for all dopant concentrations and thicknesses above 200 nm compared to the n-type. As represented in Fig. 6g, the device with n-type DS PbS ink reached its maximum PCE at 400 nm active layer thickness and 10^{13} cm^{-3} dopant concentration whereas the device with p-type ink achieved its maximum PCE performance at 300 nm and at

10^{22} cm^{-3} dopant concentration (Fig. 6h). According to our simulation results, the maximum achievable PCE for cells with p-type DS PbS inks was over 30%, while the PCE for cells using n-type DS inks was limited to 26%.

Conclusion

In summary, this study examines the potential of DS PbS CQD ink-based solar cell in various device architectures through numerical simulations. To validate our absorption spectrum and the parameters involved in our numerical simulation, we initially used the widely utilized ITO/ZnO/DS PbS ink/PbS-EDT/Au device structure as a control cell. By obtaining results that were very close to the previous reports, we demonstrated the accuracy of our simulation parameters and experimentally obtained absorption spectrum of our DS PbS inks. After a comprehensive comparative analysis performed to evaluate the effect of various HTLs and ETLs on the cell performance, we found that the best cell performance (over 20%) can be achieved with TiO_2 and MoO_3 as the ETL and HTL, respectively. This champion cell architecture was examined further for n-type and p-type ink configurations to uncover the true potential of the DS PbS ink based solar cell. It was observed that p-type inks are more resistant to increased defect density and cells with an architecture of ITO/TiO_2 (100 nm)/ p- type DS PbS ink (400 nm)/ MoO_3(50 nm)/Au can achieve PCE over 30% when the acceptor concentration is optimized at 10^{22} cm^{-3}. PbS inks with n-type characteristics are predominantly used in literature, but the performance of these QD-based devices has not yet reached the desired levels. It is widely accepted that the main reasons underlying this limitation are defects introduced during the synthesis, surface modification and device fabrication stages. On the other hand, our study suggests that p-type PbS inks are less susceptible to these defects and are therefore better candidates for the development of high-performance QD-based devices. In this context, we believe that it is of great importance to develop strategies for synthesizing p-type DS PbS inks. It is our desire that this work highlights the potential of DS PbS inks and serves as a guide for future research in this field.

Data availability

The datasets used and/or analyzed during the current study are available from the corresponding author on reasonable request.

Received: 12 June 2024; Accepted: 9 October 2024
Published online: 08 November 2024

References

1. Kagan, C. R., Lifshitz, E., Sargent, E. H. & Talapin, D. V. Building devices from colloidal quantum dots. *Sci. (1979)* 353, (2016).
2. Hicks, A. *NREL Best Research Cell Efficiencies Chart*.
3. Yuan, M., Liu, M. & Sargent, E. H. Colloidal quantum dot solids for solution-processed solar cells. *Nat. Energy* **1** (2016).
4. Zhang, J., Gao, J., Miller, E. M., Luther, J. M. & Beard, M. C. Diffusion-controlled synthesis of PbS and PbSe quantum dots with in situ halide passivation for quantum dot solar cells. *ACS Nano*. **8**, 614–622 (2014).
5. Hines, M. A. & Scholes, G. D. Colloidal PbS nanocrystals with size-tunable Near-Infrared Emission: Observation of Post-synthesis Self-narrowing of the particle size distribution. *Adv. Mater.* **15**, 1844–1849 (2003).
6. Wang, R. et al. Colloidal quantum dot ligand engineering for high performance solar cells. *Energy Environ. Sci*. **9**, 1130–1143 (2016). https://doi.org/10.1039/c5ee03887a
7. Boles, M. A., Ling, D., Hyeon, T. & Talapin, D. V. The surface science of nanocrystals. *Nat. Mater*. **15**, 141–153 (2016). https://doi.org/10.1038/nmat4526
8. Chuang, C. H. M., Brown, P. R., Bulović, V. & Bawendi, M. G. Improved performance and stability in quantum dot solar cells through band alignment engineering. *Nat. Mater.* **13**, 796–801 (2014).
9. Lu, K. et al. High-efficiency PbS Quantum-dot solar cells with greatly simplified Fabrication Processing via Solvent-Curing. *Adv. Mater.* **30** (2018).
10. Liu, M. et al. Hybrid organic-inorganic inks flatten the energy landscape in colloidal quantum dot solids. *Nat. Mater.* **16**, 258–263 (2017).
11. Ning, Z., Dong, H., Zhang, Q., Voznyy, O. & Sargent, E. H. Solar cells based on inks of n-type colloidal quantum dots. *ACS Nano*. **8**, 10321–10327 (2014).
12. Jean, J. et al. Synthesis cost dictates the commercial viability of lead sulfide and perovskite quantum dot photovoltaics. *Energy Environ. Sci.* **11**, 2295–2305 (2018).
13. Wang, Y. et al. Room-temperature direct synthesis of semi-conductive PbS nanocrystal inks for optoelectronic applications. *Nat. Commun.* **10** (2019).
14. Tom, A. E., Thomas, A., Somakumar, A. K., Kuriakose, L. & Ison, V. V. Performance enhancement of PbS quantum dot solar cells employing a hybrid solid-state ligand exchange protocol. *Thin Solid Films*. **787** (2023).
15. Zhang, X. et al. Inorganic CsPbI3 Perovskite Coating on PbS Quantum dot for highly efficient and stable infrared light converting solar cells. *Adv. Energy Mater.***8** (2018).
16. Rafique, S., Abdullah, S. M., Shahid, M. M., Ansari, M. O. & Sulaiman, K. Significantly improved photovoltaic performance in polymer bulk heterojunction solar cells with graphene oxide /PEDOT:PSS double decked hole transport layer. *Sci. Rep*. **7** (2017).
17. Li, F. et al. Matrix manipulation of directly-synthesized PbS Quantum dot inks enabled by Coordination Engineering. *Adv. Funct. Mater.* **31** (2021).
18. Choi, M. J. et al. Cascade surface modification of colloidal quantum dot inks enables efficient bulk homojunction photovoltaics. *Nat. Commun.* **11** (2020).
19. Liu, Y. et al. Merging passivation in synthesis enabling the Lowest Open-Circuit voltage loss for PbS Quantum dot solar cells. *Adv. Mater.***35** (2023).
20. Burgelman, M., Nollet, P. & Degrave, S. *Modelling Polycrystalline Semiconductor Solar Cells*. www.elsevier.com/locate/tsf
21. Kumar, S., Bharti, P. & Pradhan, B. Performance optimization of efficient PbS quantum dots solar cells through numerical simulation. *Sci. Rep.* **13** (2023).
22. Hossain, M. K. et al. Effect of Various Electron and hole transport layers on the performance of CsPbI3-Based Perovskite Solar cells: A Numerical Investigation in DFT, SCAPS-1D, and wxAMPS frameworks. *ACS Omega*. **7**, 43210–43230 (2022).
23. Touafek, N., Mahamdi, R. & Dridi, C. *Boosting the performance of Planar Inverted Perovskite Solar cells employing Graphene Oxide as HTL. Digest J. Nanomater. Biostruct*. **16**.
24. Dahal, B., Rezaee, M. D., Gotame, R. C. & Li, W. Exploring the performance of perovskite solar cells with dual hole transport layers via SCAPS-1D simulation. *Mater. Today Commun.* **36** (2023).

25. Sawicka-Chudy, P. et al. Simulation of TiO2/CuO solar cells with SCAPS-1D software. *Mater. Res. Express*. **6** (2019).
26. Raoui, Y. et al. Performance analysis of MAPbI3 based perovskite solar cells employing diverse charge selective contacts: Simulation study. *Sol. Energy*. **193**, 948–955 (2019).
27. Gan, Y. et al. Numerical investigation energy conversion performance of tin-based perovskite solar cells using cell capacitance simulator. *Energies (Basel)*. **13** (2020).
28. Yousuf, M. H., Saeed, F. & Tauqeer, H. A. Numerical Investigation of Cu 2 O as hole transport layer for high-efficiency CIGS solar cell. (2021). https://doi.org/10.20944/preprints202110.0326.v1
29. Sahoo, A. & Mangal, S. Performance analysis of tin-based perovskite solar cell with MoO3 as a HTL under a wide temperature range. *Mater. Today Proc*.https://doi.org/10.1016/j.matpr.2023.06.109 (2023).
30. Chabri, I., Oubelkacem, A. & Benhouria, Y. Numerical development of lead-free Cs2TiI6-based perovskite solar cell via SCAPS-1D; Numerical development of lead-free Cs2TiI6-based perovskite solar cell via SCAPS-1D. https://doi.org/10.1051/e3sconf/202233600050ï
31. Rahman, M. B., Noor-E-Ashrafi, N., Miah, M. H., Khandaker, M. U. & Islam, M. A. Selection of a compatible electron transport layer and hole transport layer for the mixed perovskite FA0.85Cs0.15Pb (I0.85Br0.15)3, towards achieving novel structure and high-efficiency perovskite solar cells: A detailed numerical study by SCAPS-1D. *RSC Adv.***13**, 17130–17142 (2023).
32. Liu, J. et al. A near-infrared colloidal quantum dot imager with monolithically integrated readout circuitry. *Nat. Electron.* **5**, 443–451 (2022).
33. Moulaoui, L., Bajjou, O., Najim, A., Archi, M. & Rahmani, K. Numerical simulation of the NiO as hole transport layer in CH3NH3PbBr3perovskite based-solar cell using SCAPS-1D. in *2nd International Conference on Innovative Research in Applied Science, Engineering and Technology, IRASET 2022* (Institute of Electrical and Electronics Engineers Inc., 2022). (2022). https://doi.org/10.1109/IRASET52964.2022.9737984
34. Islam, M. S. et al. Defect study and modelling of SnX3-based perovskite solar cells with SCAPS-1D. *Nanomaterials*. 11, (2021).
35. Putra, N. M. D., Sugianto, Marwoto, P., Murtafiatin, R. & Permadis, D. P. The SCAPS-1D modeling of ZnO/CdS/CdTe thin film: Analysis of thickness and stoichiometric fraction of absorber layer on solar cell performance. in *Journal of Physics: Conference Series* vol. (IOP Publishing Ltd, 2021). (1918).
36. Ait-Wahmane, Y. et al. Elsevier Ltd,. Comparison study between ZnO and TiO2in CuO based solar cell using SCAPS-1D. in *Materials Today: Proceedings* vol. 52 166–171 (2021).
37. Memari, A., Javadian Sarraf, M., Seyyed Mahdavi Chabok, S. J. & Motevalizadeh, L. Comprehensive guidance for optimizing the colloidal quantum dot (CQD) Perovskite solar cells: experiment and simulation. *Sci. Rep.* **13**, (2023).
38. Mohandes, A., Moradi, M. & Kanani, M. Numerical analysis of high performance perovskite solar cells with stacked ETLs/C60 using SCAPS-1D device simulator. *Opt. Quantum Electron.***55**, (2023).
39. Oyedele, S. O. & Aka, B. Numerical Simulation of Varied buffer layer of solar cells based on cigs. *Model. Numer. Simul. Mater. Sci.* **07**, 33–45 (2017).
40. Tan, K. et al. Controllable design of solid-state perovskite solar cells by SCAPS device simulation. *Solid State Electron.* **126**, 75–80 (2016).
41. Al-Hattab, M. et al. Numerical simulation of a new heterostructure CIGS/GaSe solar cell system using SCAPS-1D software. *Solar Energy*. **227**, 13–22 (2021). https://doi.org/10.1016/j.solener.2021.08.084
42. Santos, M. D. L. I. et al. The effect of Se/(S+Se) compositional ratios on the performance of SnS-based solar cell: a numerical simulation. *Semicond. Sci. Technol.* **35**, (2020).
43. Seok, H. J. et al. ZnO:Ga-graded ITO electrodes to control interface between PCBM and ITO in planar perovskite solar cells. *Sci. Technol. Adv. Mater.* **20**, 389–400 (2019).
44. Husna, J. et al. Numerical study of semi-transparent thin film heterojunction p-CuO/nZnO/AZO/ITO solar cells device model using SCAPS-1D. *Chalcogenide Lett.* **18**, 667–679 (2021).
45. Wang, D., Li, Y., Yang, Y., Ding, C. & Shen, Q. Unveiling of efficiency limit to fabricate high-performance PbSe quantum dot solar cells. *Sol. Energy*. **247**, 432–440 (2022).
46. Malgras, V. et al. Trap-assisted transport and non-uniform charge distribution in sulfur-rich PbS colloidal quantum dot-based solar cells with selective contacts. *ACS Appl. Mater. Interfaces*. **7**, 26455–26460 (2015).
47. Zhitomirsky, D. et al. Colloidal quantum dot photovoltaics: The effect of polydispersity. *Nano Lett.* **12**, 1007–1012 (2012).
48. Yang, G. et al. Hole transport layer selection toward efficient colloidal PbS quantum dot solar cells. *Opt. Express*. **27**, A1338 (2019).
49. Khalaf, G. M. G. et al. PbS Colloidal Quantum Dots Infrared Solar Cells: Defect Information and Passivation Strategies. *Small Sci*. (2023). https://doi.org/10.1002/smsc.202300062
50. Liu, Y. et al. Breaking the size limitation of directly-synthesized PbS Quantum dot inks toward efficient short-wavelength infrared optoelectronic applications. *Angew. Chem. Int. Ed.*https://doi.org/10.1002/anie.202300396 (2023).
51. Sunny, A., Rahman, S., Khatun, M. M., Ahmed, S. R. & Al Numerical study of high performance HTL-free CH3NH3SnI3-based perovskite solar cell by SCAPS-1D. *AIP Adv.* **11**, (2021).
52. Morschbach, M. et al. Integrated silicon schottky mixer diodes with cutoff frequencies above 1 THz. *IEEE Trans. Microwave Theory Tech.* **53**, 2013–2018 (2005).
53. F. S. Effect of the electric field on the different electrical parameters of a solar cell. *Int. J. Res. Eng. Technol.* **07**, 16–21 (2018).
54. Tariq Jan, S. & Noman, M. Influence of layer thickness, defect density, doping concentration, interface defects, work function, working temperature and reflecting coating on lead-free perovskite solar cell. *Sol. Energy*. **237**, 29–43 (2022).
55. Wahid, M. F., Howlader, M. N., Ahasan, N. & Rahman, M. M. Performance improvement of CIGS Solar cell: A Simulation Approach by SCAPS-1D. *Energy Power Eng.* **15**, 291–306 (2023).
56. Deepika, Singh, A., Verma, U. K. & Ameen, S. Optimization of lead-free materials-based perovskite solar cell using SCAPS-1D simulation. *J. Phys. Chem. Solids* **186**, (2024).
57. Noman, M. A. A., Abden, M. J. & Islam, M. A. *Germanium Telluride Absorber Layer, A Proposal for Low Illumination Photovoltaic Application Using AMPS 1D*.

Acknowledgements

The authors gratefully acknowledge the SCAPS-1D program, which was developed by Prof. Marc Burgelman's group at Gent University, Belgium, and generously made available for use. The authors thank Firdevs Aydın for her contributions to the quantum dot synthesis processes and Caner Yalçın for performing the AFM characterization. This work was supported by the Scientific and Technological Research Council of Turkey (TÜBİTAK); Project Number 123M739.

Author contributions

B.U.: visualization, investigation, writing—original draft preparation. D.A.: conceptualization, investigation, writing—reviewing, editing and supervision.

Declarations

Competing interests
The authors declare no competing interests.

Additional information
Supplementary Information The online version contains supplementary material available at https://doi.org/10.1038/s41598-024-75981-2.

Correspondence and requests for materials should be addressed to D.A.

Reprints and permissions information is available at www.nature.com/reprints.

Publisher's note Springer Nature remains neutral with regard to jurisdictional claims in published maps and institutional affiliations.

Open Access This article is licensed under a Creative Commons Attribution-NonCommercial-NoDerivatives 4.0 International License, which permits any non-commercial use, sharing, distribution and reproduction in any medium or format, as long as you give appropriate credit to the original author(s) and the source, provide a link to the Creative Commons licence, and indicate if you modified the licensed material. You do not have permission under this licence to share adapted material derived from this article or parts of it. The images or other third party material in this article are included in the article's Creative Commons licence, unless indicated otherwise in a credit line to the material. If material is not included in the article's Creative Commons licence and your intended use is not permitted by statutory regulation or exceeds the permitted use, you will need to obtain permission directly from the copyright holder. To view a copy of this licence, visit http://creativecommons.org/licenses/by-nc-nd/4.0/.

© The Author(s) 2024